Journal of Materials Chemistry A

PAPER

View Article Online
View Journal | View Issue

Cite this: J. Mater. Chem. A, 2017, 5, 641

Electrospun PVDF–TiO_2 with tuneable TiO_2 crystal phases: synthesis and application in photocatalytic redox reactions†

Jeannie Z. Y. Tan,[ab] Natalita M. Nursam,‡[ab] Fang Xia,[bc] Yen Bach Truong,[b] Ilias Louis Kyratzis,[b] Xingdong Wang[b] and Rachel A. Caruso*[ab]

Received 23rd September 2016
Accepted 26th November 2016

DOI: 10.1039/c6ta08266a

www.rsc.org/MaterialsA

Electrospinning and hydrothermal treatment were employed to fabricate polyvinylidene fluoride (PVDF)–titanium dioxide composite photocatalytic membranes with different anatase, brookite and rutile compositions. The crystal phases were manipulated by adjusting the urea : hydrochloric acid ratio and the concentration of tetrabutyl titanate in the hydrothermal solution, forming either bicrystalline or tricrystalline TiO_2. The sample with the highest photoproduction of methane from CO_2 (19.8 μmol per $g_{catalyst}$ per h) showed a low activity in the photooxidation of phenol in aqueous solution under UV irradiation. Based on the results obtained, the crystal phase composition and microstructure of the PVDF–TiO_2 greatly influenced the photocatalytic reduction of CO_2. Electron spin resonance and XRD indicated a difference in Ti^{3+} content and this is believed to affect the rate of photodegradation of phenol. This study revealed that small, controlled changes in TiO_2 phase and morphology on the electrospun PVDF produced photocatalytic membranes with distinctly different activities.

Introduction

Solar driven photocatalytic conversion of carbon dioxide in the presence of water to hydrocarbon fuels is a sustainable route to fuel production. This approach would help to alleviate the increasing concentration of atmospheric CO_2 and partly fulfil the growing demand for renewable generation of hydrocarbon fuel.[1] Developing efficient photocatalysts for solar-driven CO_2 reduction is essential in achieving this goal. However, rapid recombination of the photogenerated electron–hole pairs in the photocatalyst is a major obstruction to achieve high photocatalytic activity.[2] In order to increase the lifetime of the photogenerated electron–hole pairs, different photocatalyst synthesis approaches (*e.g.*, impurity doping, metal deposition, heterojunction construction, surface modification and carbon-based material loading)[3–13] have been widely applied. One approach that is gaining attraction is the application of different polymorphic phases of the same semiconductor.[14–17] Titanium dioxide with mixed phases is often reported to have higher photocatalytic activity than that exhibited by the pure crystalline phase of anatase, brookite or rutile.[18–20] This is because the interaction of two different crystalline phases encourages the migration of the photogenerated electron or hole, thereby leading to charge separation. Hence, the interface of the crystalline phases (*e.g.*, rutile–anatase in Evonik P25) serves as the photocatalytic 'hot-spot'.[18] Triphasic or biphasic TiO_2 mixtures have been reported to be highly photoactive for both solid–liquid and solid–gas heterogeneous photocatalysis.[21,22]

The surface modification of TiO_2 with anionic fluorine species is another means that can be used to suppress the recombination of photogenerated electron–hole pairs.[23] For instance, surface fluorinated TiO_2 exhibited superior charge separation due to the presence of surface ≡Ti–F groups that act as electron-trapping sites. However, the rate of electron transfer at the interface is decreased as the trapped electrons are tightly held by the strong electronegativity of fluorine.[24] Polarity played a similar role in the composite of TiO_2 and β-phase polyvinylidene fluoride (PVDF): a thin film of TiO_2 deposited on the electroactive β-phase PVDF revealed an enhanced charge carrier mobility, and led to enhanced photocatalytic activity.[25] Moreover, the electrostatic surface adsorption of charged dyes on a PVDF–TiO_2 composite photocatalyst can be tuned by manipulating the amount of PVDF in the sample.[26] Optimisation of the photocatalytic performance of the PVDF–TiO_2 nanofibres (NFs) by manipulating the crystal phases of TiO_2 has not yet been reported. Therefore, the photocatalytic redox reactions of crystalline, mixed TiO_2 phases in a PVDF–TiO_2 electrospun

[a]Particulate Fluids Processing Centre, School of Chemistry, The University of Melbourne, Victoria 3010, Australia. E-mail: rcaruso@unimelb.edu.au

[b]Commonwealth Scientific and Industrial Research Organisation (CSIRO) Manufacturing, Clayton, Victoria 3168, Australia

[c]School of Engineering and Information Technology, Murdoch University, Murdoch, Western Australia 6150, Australia

† Electronic supplementary information (ESI) available: XRD patterns, electron microscopy images, photomethanation yields. See DOI: 10.1039/c6ta08266a

‡ Current address: Research Center for Electronics and Telecommunication, Indonesian Institute of Science, Jalan Sangkuriang Komplek LIPI building 20 level 4, Bandung 40135 Indonesia.

composite membrane have been studied here. In order to fabricate highly distributed TiO_2 nanoparticles (NPs) within a PVDF matrix, electrospinning, which has been widely used to fabricate polymer-based NFs, was employed. Mixtures of urea and hydrochloric acid were used to manipulate the phases of TiO_2 in the PVDF NFs. The properties of the TiO_2–PVDF NFs were characterised and the photocatalytic redox reactions of the TiO_2–PVDF electrospun membranes were measured using the photooxidative degradation of phenol and photoreduction of CO_2.

Experimental

Materials

PVDF (Kynar Flex® 2801) was purchased from Arkema. *N*,*N*-Dimethylformamide (DMF, analytical grade), acetone (analytic grade), copper(II) acetate (98%), hydrochloric acid (HCl, 32% analytic grade), tetrabutyl titanate (TBT, 97% reagent grade), phenol (≥96%), *tert*-butyl alcohol (≥99.5%) and benzoquinone (≥98%) were purchased from Sigma Aldrich. Urea was purchased from BDH Chemical Ltd. All chemicals were used without further purification. A commercial TiO_2, Evonik P25 (referred to as P25 throughout the text), was used as the reference photocatalyst. Water used throughout the experiment was obtained from a Milli-Q purification system with resistivity higher than 18 MΩ cm.

Synthetic procedures

Electrospinning. PVDF powder (4.0 g) was added to a 20 mL mixture of solvents (DMF : acetone in the volume ratio of 7 : 3) and stirred vigorously for 1 h. Then, 8 mL of TBT was added and the solution was stirred for another 24 h.

Electrospinning of the PVDF–TBT solution was carried out using a 3 mL syringe with a 21 gauge needle (0.8 mm). Electrospinning parameters used were 120 mm distance between needle and grounded collection plate, 18 kV (DC voltage supply Spellman TFT 2056 mode) and a pumping rate of 2 μL min^{-1} (New Era Pump Systems, Inc) for 30 min. The electrospun membranes were collected on fluorinated tin oxide conductive coated glass (10 Ω sq^{-1} purchased from Mei Jing Yuan Glass Technology Ltd), which was subsequently placed into the Teflon reactor for hydrothermal treatment.

Hydrothermal reaction. Known amounts of TBT (refer to Table 1) were added to solutions of different ratios of aqueous urea (0.5 M) : aqueous HCl solution (5.0 M) to make a total solution volume of 20 mL. The solutions were stirred vigorously until they became clear and then transferred into a Teflon lined stainless steel autoclave (30 mL). The electrospun PVDF–TBT membrane was then added to this solution and heated at 120 °C for 24 h without stirring. After the hydrothermal reaction, the membrane was thoroughly washed with deionized water and air dried overnight.

Materials characterisation

Room temperature powder X-ray diffraction (PXRD) was conducted on a Bruker D8 Advance X-ray diffractometer using CuKα radiation. Data was analysed using a Bruker EVA™ with crystalline phases identified using the ICDD-JCPDS powder diffraction file database. Rietveld refinement using Bruker TOPAS™ was carried out to calculate the weight fraction of the phases present.

In situ PXRD experiments were conducted using the powder diffraction beamline at the Australian Synchrotron. The setup is described in detail elsewhere.[27,28] The X-ray energy was 16 keV, and the wavelength (0.7743 Å) was calibrated using a LaB_6 standard (NIST SRM 660b). Prior to the experiment, an electrospun PVDF–TBT membrane and aqueous HCl (5 M) were loaded into a quartz glass capillary (1 mm in diameter, 0.1 mm in wall thickness, and 40 mm in length), which was sealed in a custom-made stainless steel holder designed by Norby.[29] An external N_2 pressure (3 MPa) was applied to the capillary to prevent vaporisation of the solvent. The capillary was fixed at the centre of the X-ray beam and then heated (10 °C min^{-1}) to 120 °C by a hot air blower beneath the capillary. The

Table 1 Reagent composition and pH value of the hydrothermal solution used in the preparation of the PVDF–TiO_2 membrane and the crystal phase composition of the fabricated PVDF–TiO_2 membrane

	Hydrothermal solution (mL)				Crystal phase composition (%)		
Sample no.	Urea	HCl	TBT concentration (M)	pH	Anatase	Brookite	Rutile
1	20	0	0.030	6.49	96	4	0
2	20	0	0.125		90	5	5
3	19	1	0.250	0.57	83	17	0
4	19	1	0.030		73	0	27
5	18	2	0.250	0.40	64	18	18
6	18	2	0.030		64	12	24
7	17	3	0.250	0.30	55	0	45
8	17	3	0.030		46	12	42
9	16	4	0.250	0.24	39	9	52
10	16	4	0.030		12	20	68
11	15	5	0.030	<0	0	22	78
12	0	20	0.125	<0	0	0	100

temperature was monitored by a K-type thermocouple 3.5 mm beneath the capillary. *In situ* diffraction patterns were collected continuously with a time resolution of 2 min.

The sample morphology was examined by scanning electron microscopy (SEM) under high vacuum mode using a field-emission environmental SEM (Quanta 200F FEI) with a voltage of 10 kV. The samples were not pre-coated. Transmission electron microscopy (TEM) and high resolution TEM (HRTEM) images were obtained on a transmission electron microscope (FEI Tecnai F20) operated at 200 kV. The samples were prepared by placing the PVDF–TiO_2 membranes in a 2 mL ethanol solution and sonicating for 20 min. A drop of this solution was evaporated onto a holey carbon coated copper TEM grid.

Attenuated total reflectance Fourier transform infrared (ATR-FTIR) spectra were collected at room temperature using a ThermoScientific model Nicolet 6700 FT-IR with 16 acquisitions.

Electron spin resonance (ESR) spectra were measured at −196 °C using a Bruker Elexsys-II E560. Before the measurement, the PVDF–TiO_2 membrane (0.01 g) and 2 mL of copper acetate solution (0.1 M) was put into a thin wall quartz ESR tube (4 mm OD × 250 mm in length). The tube was either left in the dark or irradiated with UV light ($\lambda = 365$ nm; XX-15A, Spectroline) for 15 min then immediately immersed into liquid nitrogen until it froze. The ESR tube was carefully placed into the sample holder, which was filled with liquid nitrogen. During the measurement the modulation amplitude and phase were set at 4.00 and 0, respectively. The receiver gain was set at 10 dB with a time constant of 20.48 ms and sweep time of 100.71 s.

Thermogravimetric analysis (TGA) conducted on a Mettler Toledo TGA/SDTA-851^e instrument was used to measure the TiO_2 content of the PVDF–TiO_2 membranes. The measurement was conducted from 25 °C to 900 °C under an air environment (compressed air from Coregas, 30 mL min^{-1}) with a ramp rate of 10 °C min^{-1}.

Photocatalytic redox reactions

The photocatalytic activities of the PVDF–TiO_2 membranes were evaluated using UV irradiation by the photodecomposition of phenol and photoreduction of CO_2. UV irradiation for these experiments was supplied from two 15 W Hg UV-A black tube lamps (XX-15A, Spectroline) with a single peak wavelength at 365 nm.

Phenol photodegradation. This was evaluated using a high throughput photocatalytic screening set up. The amount of fabricated membrane (in pieces) used was 1.0 g L^{-1}, and the phenol concentration was 10 ppm. Prior to the photocatalysis experiment, samples were suspended in phenol solutions with or without *tert*-butyl alcohol (0.1 mM) and benzoquinone (0.1 mM) in a 24-well plate and shaken in the dark overnight on a medium orbital shaker (Model: OM6 from Ratek Instruments Pty. Ltd) until sorption equilibrium was achieved. During the photocatalytic reaction, the phenol concentration was monitored at 270 nm using a UV-Vis plate reader (FlexStation 3 Kinetic Plate Reader, Molecular Devices) every 0.5 h for 2.5 h. The photocatalytic activity was expressed as an apparent reaction rate constant, k, which was obtained as the mean from duplicate samples. The k value of the PVDF–TiO_2 membrane was determined from the slope of a $[\ln(C_0/C(t))]/t$ plot, where $C(t)$ is the concentration measured after t min, and C_0 is the initial concentration measured immediately before irradiation. P25 (1.0 g L^{-1}) was used as the reference material for the photocatalytic reactions. The experimental conditions and procedures were similar to those above.

The quantum efficiency for the phenol photodecomposition reaction (Q. $E._{phenol}$) was calculated using the following equation:

$$\text{Q. E.}_{\cdot\text{phenol}} = \frac{\text{rate of phenol decomposition}}{\text{absorbed photon flux at 365 nm}}$$

CO_2 photoreduction. All measurements were carried out at room temperature (25–27 °C) in a quartz photoreactor (internal diameter of 77 mm and 97 mm in depth), which was placed in a dark cabinet that was fitted with cooling fans. The PVDF–TiO_2 membrane (approx. 2 cm × 2 cm, exact mass known) was placed into the quartz reactor and was tested with a mixture of CO_2 and water that was generated by bubbling CO_2 (99.9% BOC Australia) through water (Milli-Q) in a 25 mL water bubbler. Prior to the test, the mixture of CO_2 and water was purged through the reactor at 100 mL min^{-1} for 1 h. The flow rate of the CO_2 was then decreased and maintained at 10 mL min^{-1} throughout the photoreduction test. P25 was immobilised on a microscope glass slide by placing a drop of concentrated P25 in ethanol on the slide. The coating was left in the oven (60 °C) to allow ethanol to evaporate. The concentration of the effluent gas was monitored by gas chromatography (Tracera GC-2010 Plus capillary equipped with a barrier discharge ionization detector from Shimadzu) as a function of irradiation time. The CO_2 was initially monitored in the dark to ensure no other organic substances were present or generated from the PVDF–TiO_2 samples that interfered with the CO_2 detection. After 1 h in the dark, the first gas sample was taken and analysed, and then the UV lamp was turned on and gas samples were removed and measured at 1 h intervals.

The quantum efficiency for the photomethanation reaction (Q. $E._{CH_4}$) was calculated using the following equation:

$$\text{Q. E.}_{\cdot\text{CH}_4} = \frac{\text{rate of CH}_4\text{ generation}}{\text{absorbed photon flux at 365 nm}}$$

The photon flux was recorded using a quantum efficiency test instrument (Keithley 2400 SourceMeter) under the same irradiation (two 15 W Hg UV-A black tube lamps (XX-15A, Spectroline) with a single peak wavelength at 365 nm) as used for the photocatalytic reactions.

The isotope analysis of ^{13}C was performed using the same photocatalytic setup with known amount of membrane (sample 2) and the CO_2 source was $^{13}CO_2$ (99 atom% ^{13}C from Sigma Aldrich). The analysis was conducted using gas chromatograph-mass spectroscopy (Thermo TSQ 8000 TRACE 1310).

Results and discussion

The crystal phase and structure of the PVDF membranes prior to and following hydrothermal treatment were examined and are described below.

Crystal phase composition

The XRD pattern of the PVDF–TBT membrane prior to hydrothermal treatment, as shown in Fig. S1a† reveals one intense PVDF peak (20.4°) accompanied by a shoulder peak (18.4°) and a weak peak at 36.2° (Fig. S1a†). No peak corresponding to crystallised TiO_2 was observed in the electrospun PVDF–TBT composite that had a NF microstructure (Fig. S1b†).

The urea, HCl and TBT concentrations and the pH of the different hydrothermal solutions used to treat the electrospun PVDF–TBT membranes are shown in Table 1. The highest concentration of TBT added into the urea or HCl solutions was 0.125 M, whereas in mixed solutions (*i.e.*, different ratio of urea : HCl) it was 0.250 M. This high concentration of TBT (*i.e.*, 0.250 M) in urea caused the growth of TiO_2 in the solution rather than stimulating the growth of TiO_2 within the PVDF, giving poorly crystalline TiO_2 in the membrane. Contrastingly, the HCl solution induced heavy growth of TiO_2 on the PVDF NFs, which tended to detach. However, when low TBT concentrations (*i.e.*, 0.030 M) were used in urea or HCl solution, TiO_2 NPs grew on the NFs during the hydrothermal treatment (further discussion can be found in the microstructure section).

The pH of the hydrothermal solutions, as shown in Table 1, decreased with increasing HCl content. The TiO_2 phase composition in the PVDF–TiO_2 membrane could be finely tuned even in such a highly acidic environment. To determine which crystalline phases of TiO_2 were present in the fabricated PVDF–TiO_2 membranes, room temperature PXRD patterns were obtained (Fig. S2a†). After Rietveld refinement, the weight fractions of the crystalline phases were calculated, and are summarised in Table 1 (a graphical form of this data is available in Fig. S2b†). Except for sample 12, which was entirely rutile, all other samples were biphasic or triphasic TiO_2. Brookite, if present, was always a minor fraction. The overall trend of the TiO_2 phases showed that the anatase fraction of the membranes decreased with a decrease in the urea : HCl ratio. For samples 9 to 12, rutile became the predominant phase due to the high acidity of the hydrothermal solutions favouring the growth of rutile.[30,31]

Different morphologies and crystal phase compositions of the TiO_2 were obtained and strongly depended on the amount of TBT used and the pH of the hydrothermal solution. In an aqueous urea solution, anatase was the predominant phase (96%) with the formation of 4% brookite in sample 1, and 5% each of brookite and rutile in sample 2. For these two hydrothermal solutions, the solution pH was the same (pH 6.49) but the TBT concentrations of the hydrothermal solutions were different, 0.030 and 0.125 M. As a precipitate was formed on the addition of TBT to the urea solution when pH > 1, the growth of TiO_2 *via* dissolution and crystallisation was expected to be negligible.[32] The formation of rutile in sample 2 is due to the increase in TBT concentration. A low TBT concentration in the urea solution promotes the heterogeneous nucleation of anatase and a trace amount of brookite, the high concentration of TBT might have induced the crystallisation of rutile at the interfaces between anatase crystals, which serve as potential nucleation sites for rutile grain growth as proposed previously.[33]

When the urea : HCl ratio decreased, the anatase component decreased and the rutile phase increased (Table 1) as the corresponding reduction in pH favoured the rutile formation. The high acidity of the hydrothermal solutions, as for samples 9 to 11, resulted in rutile becoming the predominant phase;[30,31] and eventually only the rutile phase was obtained in sample 12. In addition, the high HCl concentration caused anisotropic growth of rutile as evidenced in the synchrotron *in situ* PXRD (Fig. 1). At the beginning of the synthesis, a broad amorphous peak (5–15°) was observed. This broad peak was due to the simultaneous contribution of three components (*i.e.*, quartz glass capillary, hydrothermal solution and the Ti-precursor). Since the amorphous nature of quartz glass capillary and the hydrothermal solution would not change in the *in situ* experiment, the loss in intensity at around 11° 2θ with time is associated with the dissolution of the amorphous Ti-precursor. The first 20 minutes is an induction period for nucleation since no crystalline peaks are obvious. Once crystallisation commences, the intensity of the rutile peaks rises gradually. The sharp peak at approximately 27.3° 2θ suggested the particles were elongated along the [001] crystal direction.

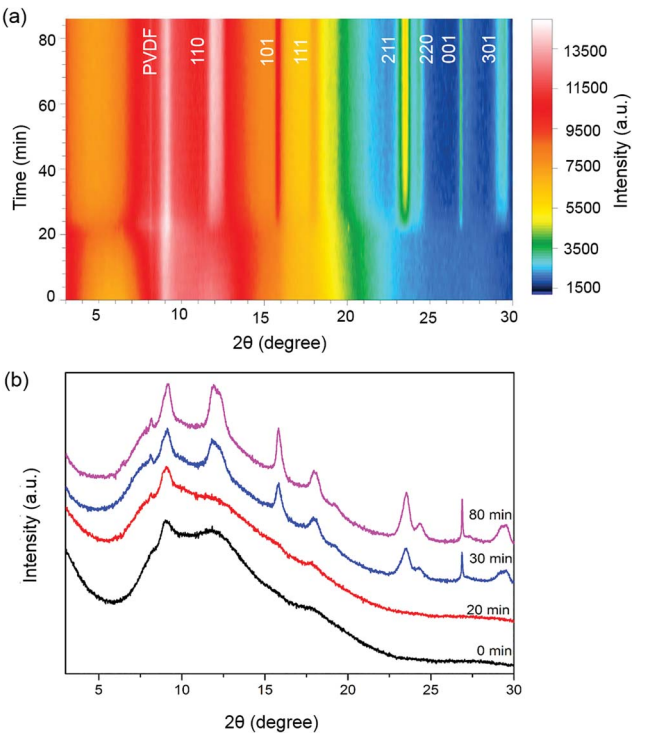

Fig. 1 Synchrotron *in situ* PXRD pattern of PVDF–TiO_2 membrane (sample 12) in 5 M HCl (a). Each peak in the PXRD pattern was labelled with the corresponding *hkl*. Selected synchrotron PXRD patterns at 0, 20, 30 and 80 min (b).

Interaction between TiO_2 and PVDF

The room temperature PXRD of the PVDF and TiO_2–PVDF samples indicated the presence of both the PVDF α and/or γ and β crystalline phases after hydrothermal treatment (Fig. S2a†). A broad peak at 18.5° and a much more intense peak at 20.7° can be attributed to the α and/or γ[34] and β phases,[35] respectively. Due to the overlap of the α and γ phases in the PXRD, further analysis was conducted using IR spectroscopy as shown in Fig. 2. The spectra of PVDF before and after hydrothermal treatment showed that α (763 and 970 cm^{-1}) and β (839 and 1273 cm^{-1}) phases were present, while the γ phase (1234 cm^{-1}) was absent.[34] A mixture of α and β phases were observed in all the hydrothermally treated PVDF–TiO_2 samples (Fig. 2).

The relative intensity of the β phase varied for the samples, with samples 1 to 6 having higher relative intensity compared to pristine PVDF, while from sample 7 onwards the intensity decreased gradually. The increase in the relative intensity of the β phase peaks from samples 1 to 6 is believed to be independent of the hydrothermal treatment process (compare (i) and (ii) in Fig. 2), but is instead affected by the NPs grown on the NFs, as observed previously by Andrew *et al.*[36] They found that the increase in the β phase can be explained by the size of NPs that are present on the electrospun NFs according to the expanded Flory mixing theory developed by Mackay *et al.*[37] Using this theory, Mackay and co-workers demonstrated that dispersed NPs could cause the polymer to swell when the radius of the NPs was less than the radius of gyration, R_g, of the polymer. According to Andrew *et al.*, the R_g of PVDF based on the freely jointed chain model,[36] was 27.5 nm,[37] which is much greater than the mean diameter of the TiO_2 NPs grown here on the PVDF NFs. The NP size distribution was determined for samples 2, 3, 4, and 5, the majority being less than 27.5 nm (Fig. S3†). The TiO_2 NP size for sample 1 could not be measured due to agglomeration of TiO_2 NPs within the electrospun NFs, whereas for sample 6, heavy growth as well as self-assembled nanorods on the PVDF NFs prevented accurate determination of NP size. The measured NP size was less than the R_g of PVDF, therefore the increased intensity of the β phase in the IR result could be due to the presence of TiO_2 NPs. According to Andrew *et al.*,[36] it could be that when the TiO_2 NPs nucleated and grew within the PVDF NFs, the polymer swelled, thus increasing its R_g. The increase of R_g was manifested by intensifying the crystalline β phase of the PVDF membranes, samples 1 to 6, as shown in Fig. 2. When the growth of TiO_2 NPs was promoted further with the reduction in the urea : HCl ratio of the hydrothermal solutions, as for samples 7 to 12, the size of TiO_2 NPs became larger than the R_g of PVDF. Therefore, a reduced β phase intensity was observed in the IR spectra (Fig. 2).

The urea : HCl volume ratio of the hydrothermal solutions also affected the PVDF : TiO_2 weight ratio (Table S1†) in the final membrane. The overall trend showing a decrease in PVDF content with reducing urea : HCl ratio.

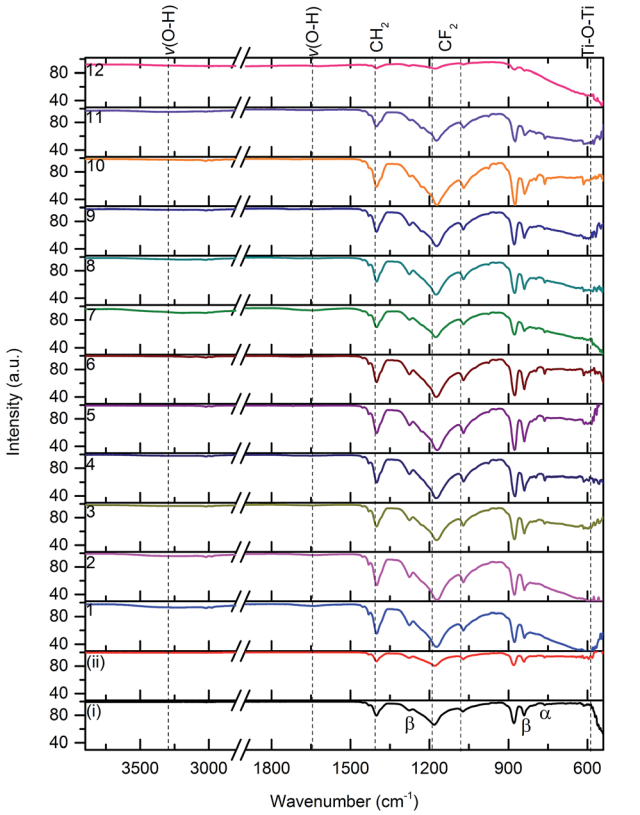

Fig. 2 IR spectra of pure PVDF before (i) and after (ii) hydrothermal treatment and the PVDF–TiO_2 membranes, labelled by sample number (1–12).

Microstructure

The microstructure of the electrospun PVDF–TiO_2 membranes was studied by SEM and TEM. Prior to the hydrothermal treatment, TBT was trapped in the middle of the electrospun NFs (Fig. S1b†), which is in agreement with a previous report.[38] In order to simplify the discussion of this work, the following discussion will focus on four representative samples, namely samples 1, 2 (a low and high concentration of TBT in alkaline hydrothermal solutions), 7 and 9 (having intermediate urea : HCl ratios with same concentration of TBT). SEM images show that the NFs of samples 1 and 2 are relatively smooth (Fig. 3a and b) and free of external TiO_2 NPs, while TEM revealed that crystallised TiO_2 NPs were present within the NFs (Fig. 3e and f). As mentioned earlier, precipitate was formed when the hydrothermal solution has a pH > 1, thus, the TiO_2 crystallisation of sample 1 and 2 only occurred within the NFs. TiO_2 NPs with lattice fringes of 3.53 Å, assigned to anatase, were agglomerated at the centre of the electrospun NFs (Fig. 3i).

Sample 2 was hydrothermally treated in a higher TBT concentration (0.125 M) solution than sample 1. Sample 2 shows agglomeration of TiO_2 at the centre of the NFs as well as discrete and dispersed TiO_2 NPs near the edge of the NFs (Fig. 3f). HRTEM of TiO_2 NPs at the edge of the fibre exhibited lattice fringes that were assigned to rutile (3.25 Å) and anatase (3.53 Å) (Fig. 3j). Such an observation could suggest that the formation of rutile in this sample was through interfacial nucleation.

When the pH of the hydrothermal solutions decreased to below 1, TiO_2 particles grew on the surfaces of the NFs without

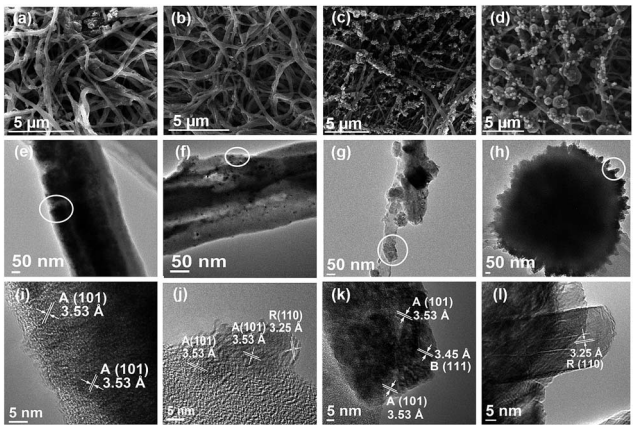

Fig. 3 SEM images of four representative electrospun PVDF–TiO_2 membrane samples 1, 2, 7 and 9 (a–d). Corresponding TEM (e–h) and HRTEM images (i–l) of the circled areas in (e–h) labelled with the lattice fringes of anatase (A), brookite (B) and rutile (R).

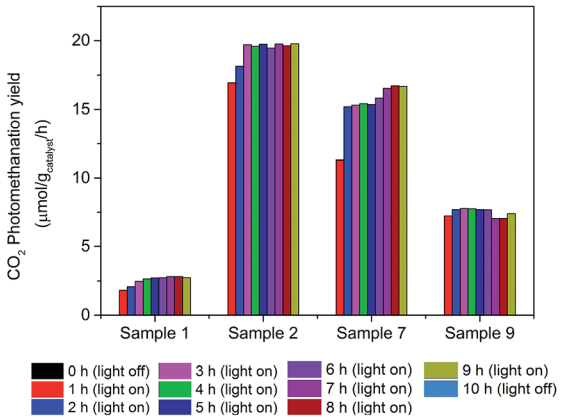

Fig. 4 The CO_2 photomethanation yield over 11 h (with 1 h in the dark, 9 h under UV irradiation and another 1 h in the dark) of four representative PVDF–TiO_2 samples (sample 1, 2, 7 and 9).

agglomeration at the core of the NFs (Fig. 3c, d and S4†). The dissolution of TBT within the electrospun fibre, which was shown in the synchrotron *in situ* PXRD experiment (Fig. 1), induces the TiO_2 NP formation on the surface of the electrospun NFs (Fig. 3c, d and S4†). Interestingly, only anatase (3.53 Å) and brookite (3.45 Å) crystals were observed on the NFs of sample 7 (Fig. 3k). A few "sea urchin"-like particles were found detached from the NFs in this sample. These large particles were made up of agglomerated rutile nanorods, similar to the spherical agglomerates obtained from sample 8, 9 and 12 (Fig. S4i, 3h and S4l, respectively†), as indicated by the rutile lattice fringes (3.25 Å). The nanorods were elongated along the [001] crystal direction (Fig. 3l), which was evidenced in the sharp and narrow (001) peak at ~27.3° 2θ in the *in situ* PXRD pattern (Fig. 1b).

Photocatalytic reduction of CO_2

The photoreduction of CO_2 to methane (or photomethanation), was used to analyse the photocatalytic activities of the PVDF–TiO_2 membranes against the P25 control. The photoreduction of CO_2 under UV irradiation was conducted for 9 h (with the samples kept in the dark for an initial and final hour) and the reaction was monitored by the production of methane (Fig. 4 and S5†). When illuminated the photoproduction of methane was observed for all samples except the P25 control, which had no detectable methane yield. Methanation did not occur in the dark (without illumination) for any sample. These results agree with previously reported work, showing no activity when the photocatalyst was not illuminated and limited or no yield using P25 as the photocatalyst.[7]

Sample 1 had the lowest CO_2 photomethanation activity (rate = 2.7 μmol per $g_{catalyst}$ per h and Q. $E._{CH_4}$ = 0.06%), whereas sample 2 had the highest CO_2 photomethanation rate at 19.8 μmol per $g_{catalyst}$ per h (Fig. 4) and Q. $E._{CH_4}$ = 0.44% under UV irradiation. The superior methane production in sample 2 over sample 1 was probably due to the TiO_2 NPs being accessible on the surface of the NF that allowed the adsorption of CO_2 directly on the TiO_2 NPs for electron injection into CO_2 molecules, subsequently reducing CO_2 to methane (Fig. 3j). When the size of TiO_2 NPs increased with lower urea : HCl ratio, the photomethanation rates decreased dramatically (Fig. 4 and S5† for sample 3–6). Although the size of the NPs in sample 7 was larger than that in samples 3–6, the photomethanation yield of sample 7 was much higher than that in samples 3–6 but slightly lower than sample 2. In this case, it was believed that the effect of crystal phase composition played a significant role in determining the photomethanation activity. Sample 7 contained 55% anatase, which is reported to contain a potential site for CO_2 activation and 45% rutile, which has an effective reduction site.[39,40] Therefore, having anatase and rutile in about the same ratio shows enhanced photomethanation activity. Further increasing the rutile composition (samples 8–12) induced a low photomethanation yield. In addition, a low percentage (12%) or an absence of the anatase phase significantly delayed the methane production upon UV irradiation (samples 10–12, Fig. S5†), as methane was only detected after the second (sample 10) and third hour (samples 11 and 12) of irradiation. Based on these results, the photomethanation activity of PVDF–TiO_2 was significantly affected by both the crystal phase composition and microstructure of the photocatalyst. Correlation between the PVDF amount and the photocatalytic methanation activity of the PVDF–TiO_2 membranes was not observed.

The photoreduction of CO_2 was further investigated using isotope labelled $^{13}CO_2$ (m/z = 45.024) and $^{12}CO_2$ (m/z = 44.020), which photoproduced $^{13}CH_4$ (m/z = 17.016) and $^{12}CH_4$ (m/z = 16.015), respectively (Fig. S6†). The intensity ratio of $^{13}CH_4$ matches that of $^{12}CH_4$. Hence, the main organic product was verified to be generated from the reduction of $^{13}CO_2$.

The PVDF–TiO_2 samples that exhibited the highest (sample 2) and lowest (sample 1) CO_2 photomethanation were tested for aqueous phase phenol photodegradation (Fig. 5). The photodegradation activity of these two samples shows a reverse performance to their photomethanation activities. Sample 1 (Q. $E._{phenol}$ = 0.50%) exhibited a higher photodegradation

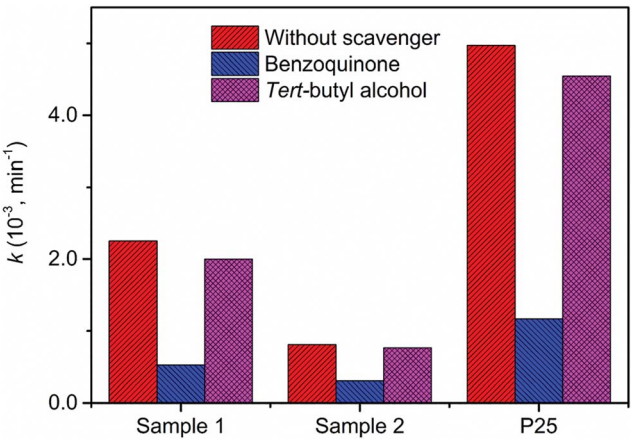

Fig. 5 Phenol photodegradation of sample 1, 2 and P25 under UV irradiation.

activity than sample 2 (Q. $E._{phenol} = 0.18\%$). To understand the underlying reaction mechanism involved in the photocatalytic degradation of phenol, a series of control experiments was conducted (Fig. 5). As shown in Fig. 5, when benzoquinone (scavenger of $O_2^{\bullet -}$) was added, the phenol photodegradation activity of sample 1 and 2 was significantly inhibited. When *tert*-butyl alcohol, which scavenges $OH^{\bullet}$, was added, the phenol photodegradation activity was not affected significantly. These results indicated that $O_2^{\bullet -}$ played a vital role in catalysing the photodecomposition of phenol in aqueous solution under the irradiation of UV. In this respect, a direct interaction is not required to undergo the photodecomposition of phenol, therefore, the PVDF layer did not inhibit the photocatalytic activity of phenol decomposition in sample 1. This is similar to a previous observation, where the radical species diffused through a Nafion layer and subsequently decomposed the organic molecules.[41]

Comparing sample 1 and 2, the phenol photodegradation of these samples possibly correlates to the amount of bulk Ti^{3+} ($g \approx 1.99$, Fig. S7a†),[42] which provides two advantages to the photodecomposition of phenol under UV irradiation.[43] Firstly, the bulk Ti^{3+} could effectively serve as an acceptor of the photogenerated electrons to suppress the charge recombination of photogenerated electron–hole pairs.[44] Secondly, the bulk Ti^{3+} in the titania material increased the chemisorption of the oxygen species, which is beneficial for the oxidative photodegradation activity.[45] In the ESR results, Fig. S7a,† similarly intense axial signals at $g \approx 1.99$ for samples 1 and 2 were detected. However, a narrower line width was observed in sample 2 due to a lower concentration of Ti^{3+} centres.[46,47] A lower PXRD peak intensity centred at 42.8° was also indicative of this difference in Ti^{3+} concentration (Fig. S7b†). Therefore, the low phenol photodegradation activity in sample 2 was due to the lower quantities of bulk Ti^{3+} being present compared with sample 1. The intense ESR signal at $g \approx 2.04$, which was assigned to the paramagnetic β-phase of PVDF,[48] was present in both samples 1 and 2 but absent in the blank $Cu(CH_3COO)_2$ (Fig. 5b).

Conclusions

Free standing PVDF–TiO_2 membranes with single, bi- or tri-crystalline titania phases were fabricated using a combined electrospinning and hydrothermal treatment method. The phase composition of anatase, brookite and rutile was finely tuned by manipulating the ratio of urea and HCl in the hydrothermal solutions. When the electrospun membrane was hydrothermally treated in a urea solution, anatase was the predominant phase and TiO_2 NPs were agglomerated at the centre of the electrospun NFs. When the acidity of the hydrothermal solutions increased, TiO_2 NPs were formed on the surface of the NFs and the anatase fraction of the membranes decreased. Brookite, if present, was always a minor fraction.

CO_2 photoreduction on the PVDF–TiO_2 membranes was influenced by the crystal phase and microstructure of TiO_2 within the electrospun PVDF NFs. The PVDF–TiO_2 sample with the highest photoreduction activity (sample 2) showed a relatively low photooxidation activity towards phenol. This was due to a lower concentration of photoinduced Ti^{3+} being present in sample 2 compared to sample 1.

Acknowledgements

This research was supported by the CSIRO Office of the Chief Executive (OCE) Science Leader and Postdoctoral Fellow schemes. The *in situ* PXRD was conducted on the powder diffraction beamline at the Australian Synchrotron, Victoria, Australia. Room temperature PXRD analysis was conducted by Dr Aaron Seeber at CSIRO Manufacturing. The Melbourne Advanced Microscopy Facility of the University at Melbourne (UoM) is acknowledged for access to SEM and TEM. ESR measurements were conducted by Mrs Sioe See Volaric at the School of Chemistry, UoM. Jeannie Z. Y. Tan acknowledges UoM for a Melbourne International Fee Remission Scholarship (MIFRS) and a Melbourne International Research Scholarship (MIRS).

Notes and references

1 E. V. Kondratenko, G. Mul, J. Baltrusaitis, G. O. Larrazabal and J. Perez-Ramirez, *Energy Environ. Sci.*, 2013, **6**, 3112–3135.
2 Y.-P. Yuan, L.-W. Ruan, J. Barber, S. C. Joachim Loo and C. Xue, *Energy Environ. Sci.*, 2014, **7**, 3934–3951.
3 M. S. Akple, J. Low, Z. Qin, S. Wageh, A. A. Al-Ghamdi, J. Yu and S. Liu, *Chin. J. Catal.*, 2015, **36**, 2127–2134.
4 Y. Li, W. Zhang, X. Shen, P. Peng, L. Xiong and Y. Yu, *Chin. J. Catal.*, 2015, **36**, 2229–2236.
5 M. Tahir, B. Tahir, N. A. Saidina Amin and H. Alias, *Appl. Surf. Sci.*, 2016, **389**, 46–55.
6 T. Wang, X. Meng, G. Liu, K. Chang, P. Li, Q. Kang, L. Liu, M. Li, S. Ouyang and J. Ye, *J. Mater. Chem. A*, 2015, **3**, 9491–9501.
7 W.-N. Wang, W.-J. An, B. Ramalingam, S. Mukherjee, D. M. Niedzwiedzki, S. Gangopadhyay and P. Biswas, *J. Am. Chem. Soc.*, 2012, **134**, 11276–11281.

8 J. Yu, J. Low, W. Xiao, P. Zhou and M. Jaroniec, *J. Am. Chem. Soc.*, 2014, **136**, 8839–8842.
9 W. Yu, D. Xu and T. Peng, *J. Mater. Chem. A*, 2015, **3**, 19936–19947.
10 X. Pan and Y.-J. Xu, *J. Phys. Chem. C*, 2015, **119**, 7184–7194.
11 L.-L. Tan, W.-J. Ong, S.-P. Chai, B. T. Goh and A. R. Mohamed, *Appl. Catal., B*, 2015, **179**, 160–170.
12 Z. He, J. Tang, J. Shen, J. Chen and S. Song, *Appl. Surf. Sci.*, 2016, **364**, 416–427.
13 Y. Yang, M. Qiu and L. Liu, *Ceram. Int.*, 2016, **42**, 15081–15086.
14 M. Yan, F. Chen, J. Zhang and M. Anpo, *J. Phys. Chem. B*, 2005, **109**, 8673–8678.
15 J. C. Yu, J. Yu, W. Ho and L. Zhang, *Chem. Commun.*, 2001, 1942–1943.
16 T. Ohno, K. Tokieda, S. Higashida and M. Matsumura, *Appl. Catal., A*, 2003, **244**, 383–391.
17 L. Chen, M. E. Graham, G. Li, D. R. Gentner, N. M. Dimitrijevic and K. A. Gray, *Thin Solid Films*, 2009, **517**, 5641–5645.
18 D. C. Hurum, A. G. Agrios, K. A. Gray, T. Rajh and M. C. Thurnauer, *J. Phys. Chem. B*, 2003, **107**, 4545–4549.
19 T. Ozawa, M. Iwasaki, H. Tada, T. Akita, K. Tanaka and S. Ito, *J. Colloid Interface Sci.*, 2005, **281**, 510–513.
20 P. Ruan, J. Qian, Y. Xu, H. Xie, C. Shao and X. Zhou, *CrystEngComm*, 2013, **15**, 5093–5099.
21 A. Di Paola, M. Bellardita and L. Palmisano, *Catalysts*, 2013, **3**, 36–73.
22 G. Tian, H. Fu, L. Jing, B. Xin and K. Pan, *J. Phys. Chem. C*, 2008, **112**, 3083–3089.
23 Y. Wang, L. Li, X. Huang, Q. Li and G. Li, *RSC Adv.*, 2015, **5**, 34302–34313.
24 H. Park and W. Choi, *J. Phys. Chem. B*, 2004, **108**, 4086–4093.
25 C. J. Tavares, S. M. Marques, L. Rebouta, S. Lanceros-Méndez, V. Sencadas, C. M. Costa, E. Alves and A. J. Fernandes, *Thin Solid Films*, 2008, **517**, 1161–1166.
26 L. Ye, C. Yang, L. Tian, L. Zan and T. Peng, *Appl. Surf. Sci.*, 2011, **257**, 8072–8077.
27 F. Xia, D. Chen, N. V. Y. Scarlett, I. C. Madsen, D. Lau, M. Leoni, J. Ilavsky, H. E. A. Brand and R. A. Caruso, *Chem. Mater.*, 2014, **26**, 4563–4571.
28 W. Li, F. Xia, J. Qu, P. Li, D. Chen, Z. Chen, Y. Yu, Y. Lu, R. Caruso and W. Song, *Nano Res.*, 2014, **7**, 903–916.
29 P. Norby, *J. Am. Chem. Soc.*, 1997, **119**, 5215–5221.
30 Z. Lai, F. Peng, H. Wang, H. Yu, S. Zhang and H. Zhao, *J. Mater. Chem. A*, 2013, **1**, 4182–4185.
31 J.-G. Li, T. Ishigaki and X. Sun, *J. Phys. Chem. C*, 2007, **111**, 4969–4976.
32 D. Reyes-Coronado, G. Rodríguez-Gattorno, M. E. Espinosa-Pesqueira, C. Cab, R. D. Coss and G. Oskam, *Nanotechnology*, 2008, **19**, 145605–145614.
33 H. Zhang and J. F. Banfield, *J. Mater. Res.*, 2000, **15**, 437–448.
34 B. S. Ince-Gunduz, R. Alpern, D. Amare, J. Crawford, B. Dolan, S. Jones, R. Kobylarz, M. Reveley and P. Cebe, *Polymer*, 2010, **51**, 1485–1493.
35 T. Lei, X. Cai, X. Wang, L. Yu, X. Hu, G. Zheng, W. Lv, L. Wang, D. Wu, D. Sun and L. Lin, *RSC Adv.*, 2013, **3**, 24952–24958.
36 J. S. Andrew and D. R. Clarke, *Langmuir*, 2008, **24**, 8435–8438.
37 M. E. Mackay, A. Tuteja, P. M. Duxbury, C. J. Hawker, B. Van Horn, Z. Guan, G. Chen and R. S. Krishnan, *Science*, 2006, **311**, 1740–1743.
38 J. Z. Yie Tan, J. Zeng, D. Kong, J. Bian and X. Zhang, *J. Mater. Chem.*, 2012, **22**, 18603–18608.
39 H. He, P. Zapol and L. A. Curtiss, *J. Phys. Chem. C*, 2010, **114**, 21474–21481.
40 T. A. Kandiel, R. Dillert, A. Feldhoff and D. W. Bahnemann, *J. Phys. Chem. C*, 2010, **114**, 4909–4915.
41 W. Kim, T. Tachikawa, G.-H. Moon, T. Majima and W. Choi, *Angew. Chem., Int. Ed.*, 2014, **53**, 14036–14041.
42 B. Han and Y. H. Hu, *J. Phys. Chem. C*, 2015, **119**, 18927–18934.
43 R. F. Howe and M. Gratzel, *J. Phys. Chem.*, 1985, **89**, 4495–4499.
44 F. Zuo, K. Bozhilov, R. J. Dillon, L. Wang, P. Smith, X. Zhao, C. Bardeen and P. Feng, *Angew. Chem., Int. Ed.*, 2012, **51**, 6223–6226.
45 Y. Liu, J. Wang, P. Yang and K. Matras-Postolek, *RSC Adv.*, 2015, **5**, 61657–61663.
46 A. M. Czoska, S. Livraghi, M. Chiesa, E. Giamello, S. Agnoli, G. Granozzi, E. Finazzi, C. D. Valentin and G. Pacchioni, *J. Phys. Chem. C*, 2008, **112**, 8951–8956.
47 D. G. Calatayud, T. Jardiel, M. Peiteado, F. Illas, E. Giamello, F. J. Palomares, D. Fernández-Hevia and A. C. Caballero, *J. Phys. Chem. C*, 2015, **119**, 21243–21250.
48 S. R. Allayarov, T. A. Konovalova, A. Waterfield, A. L. Focsan, V. Jackson, R. Craciun, L. D. Kispert, J. S. Thrasher and D. A. Dixon, *J. Fluorine Chem.*, 2006, **127**, 1294–1301.